



GNSS Radio Occultation Soundings from Commercial Off-the-Shelf Receivers Onboard Balloon Platforms

Kevin J. Nelson¹, Feiqin Xie¹, Bryan C. Chan², Ashish Goel², Jonathan Kosh², Tyler G. R. Reid², Corey R. Snyder², and Paul M. Tarantino²

¹Texas A&M University - Corpus Christi, Corpus Christi, TX

²Night Crew Labs, LLC, Woodside, CA

Correspondence: Kevin J. Nelson (knelson12@islander.tamucc.edu)

Abstract. The Global Navigation Satellite System (GNSS) radio occultation (RO) technique has proven to be an effective tool for Earth atmosphere profiling. Traditional spaceborne RO satellite constellations are expensive with relatively low sampling rates for individual satellites. Airborne RO platforms can provide much higher spatial and temporal sampling of ROs around regional weather events. This paper explores the capability of a low-cost and scalable Commercial-Off-The-Shelf (COTS) GNSS receiver onboard high-altitude balloons. The refractivity retrievals from balloon-borne RO payloads obtained from two flight campaigns (World View and ZPM-1) are presented. The balloon-borne RO soundings from the World View campaign show high-quality refractivity profiles in the troposphere with near-zero median difference (~2.3% median-absolute-deviation) from the colocated ECMWF ERA5 reanalysis data. Soundings from the ZPM-1 campaign show a relatively large positive bias (~2.5%). In summary, the low-cost COTS RO payloads onboard balloon platforms are worth further improvement for dense targeted atmospheric soundings to improve regional weather forecasts.

1 Introduction

The radio occultation (RO) atmospheric profiling method was first developed to measure planetary atmospheres in our solar system. The first major use of RO was part of the mission to examine atmospheric profiles of Venus as part of the Mariner V mission launched in 1967 (Fjeldbo and Eshleman, 1969; Fjeldbo et al., 1971). Due to atmospheric density change, Radio signals transmitted from the spacecraft will bend and be slightly delayed when passing through the limb of the planetary atmosphere before arriving at the receiver on Earth. This bending accumulation along the ray path can be precisely measured using excess phase delay, and can be used to derive atmospheric pressure, temperature, and concentration of atmospheric constituents (e.g., carbon dioxide concentrations on Venus). The same method was later applied to Mars (Kliore et al., 1972; Lindal et al., 1979) and Neptune (Lindal, 1992). Even as recently as 2017, additional RO missions to Venus were underway (Imamura et al., 2017).

It was not until the late 1990s that scientists began to apply RO techniques to the Earth's atmosphere using Global Navigation Satellite System (GNSS) signals as transmitting sources (Kursinski et al., 1996, 1997; Ware et al., 1996). To date, most Earth GNSS RO observations are taken from low-Earth orbiting (LEO) satellite constellations e.g., (COSMIC-1, Anthes et al., 2008), (GRAS, Luntama et al., 2008), and (COSMIC-2, Schreiner et al., 2020). More recently, several private companies



(e.g., SPIRE, GeoOptics, Planet IQ) launched CubeSat constellations that can offer RO soundings with comparable quality to the more sophisticated satellite RO missions such as both COSMIC missions (Bowler, 2020). The impact of spaceborne RO profile assimilation on global weather forecasts has been ranked second among satellite measurements (Gelaro, 2011), with its impact varying depending on assimilation methods (Boullot et al., 2014; Harnisch et al., 2013; Ruston and Healy, 2020).

RO observations are also possible from receivers inside the atmosphere, as opposed to the LEO receivers in space. One of the more common in-atmosphere RO platforms is an airplane or drone. Airborne radio occultation (ARO) typically uses custom-built receiver payloads onboard a modified aircraft with additional antennae and is capable of significantly higher spatial sampling density than spaceborne RO (Wang et al., 2016). ARO platforms have the benefit of providing on-demand RO profiles around transient weather events such as mid-latitude or tropical cyclones. A spaceborne occultation typically lasts slightly over a minute, whereas a typical ARO event takes approximately 20-30 minutes due to slower receiver velocities (Xie et al., 2008). ARO is limited primarily by flight restrictions regulated by the U.S. Federal Aviation Administration, and by fuel range of the aircrafts.

Early ARO studies developed and tested research instruments as a baseline for in-atmosphere RO, as well as modified the traditional spaceborne retrieval algorithms (Xie et al., 2008; Garrison et al., 2007; Zuffada et al., 1999; Healy et al., 2002). Open-loop signal tracking was successfully implemented recently to reduce unwrapping and tracking errors from airborne platforms (Murphy et al., 2015; Wang et al., 2016). Radio-holographic retrieval methods, such as the full-spectrum-inversion (FSI, Adhikari et al., 2016) and phase matching (PM, Wang et al., 2017), were also implemented to improve upon geometric optics retrievals in the moist lower troposphere due to multi-path errors.

Another option for an RO observation platform is a high-altitude balloon, but few attempts have been successfully implemented thus far. The Concordiasi Project (Rabier et al., 2010, 2013) is the only past field campaign during which balloon-borne RO (BRO) observations as part of the overall research goal. Haase et al. (2012) detailed the proof-of-concept BRO payload and platform design, along with some preliminary results indicating the feasibility of BRO measurements. Other remote sensing projects have used balloon platforms for other purposes (e.g., GNSS Reflectometry, Carreno-Luengo et al., 2016) but GNSS RO payloads on balloon platforms are still underrepresented.

Balloon-borne RO has many advantages over spaceborne RO and ARO. Like ARO observations, BRO platforms move slowly compared to spaceborne platforms, and are therefore capable of offering high spatial and temporal sounding densities. Additionally, BRO platforms can remain aloft and collect observations for weeks to months, depending on the design and capabilities of the platforms (Chan et al., 2022, 2021). BRO platforms can also be tactically launched *en masse* above and around transient weather events such as tropical cyclones and supercell thunderstorms to provide spatially dense sampling of atmospheric thermodynamic profiles inside and surrounding dangerous weather events.

The remainder of this paper is structured as follows. Section 2 briefly introduces a newly developed, low-cost and scalable commercial-off-the-shelf (COTS) GNSS receiver onboard high-altitude balloon and the associated flight campaigns, along with the detailed description on BRO data and methodology. Section 3 shows the refractivity retrieval process and quality control procedures based on one representative BRO case. Section 4 examines the overall statistics of the BRO observations and provides a preliminary error analysis. Finally, conclusions and future studies are summarized in Section 5.



2 Data and Methodology

60 2.1 Balloon-Borne GNSS RO Payload and the High-Altitude Balloon Platforms

A detailed description of the balloon-borne GNSS RO payload developed by Night Crew Labs (NCL) can be found in Chan et al. (2022) and Chan et al. (2021) – a summary is presented here. The instrumentation is comprised of two major components: a mission system support component, and a science payload for GNSS RO profiling. The Balloon Re-Programmable Integrated Computer (BRIC) is a third-generation flight management computer supporting data logging as well as power management, flight control, and thermal control. The GNSS Radio Occultation and Observable Truth (GROOT) is a first-generation balloon-borne GNSS RO science instrument based on commercial off-the-shelf (COTS) GNSS equipment. The GROOT payload includes a Swift Navigation Piksi Multi GNSS receiver for raw RO measurements (e.g., carrier phase, SNR, and Doppler velocities), a Trimble BX992 dual-antenna GNSS receiver coupled with an inertial navigation system and an L-band correction service, in addition to the BRIC flight computer and other ancillary needs. All balloon-borne RO data described in this study were collected from the GROOT payload. The Piksi GNSS RO receiver is particularly noteworthy, as it is about the size of a credit card, which is quite small compared to most other custom-built GNSS RO receivers for airborne and spaceborne observations.

In this study, the RO profiles collected from two high-altitude balloon flight campaigns equipped with the GROOT payload were analyzed. Figure 1a shows the GROOT payload as described above, with each component labeled. The first of a series of high-altitude balloon campaigns occurred in August 2020 on a zero-pressure balloon as a secondary payload hosted on the World View Stratolite balloon bus platform (Fig. 1b, c). The World View flight launched out of Page, AZ and maintained 18+ km (60,000+ ft) altitude, enabling five days (120 hours) of continuous data collection. During the flight, GROOT continuously collected balloon state data and RO data from the GPS (United States), GLONASS (Russia), Galileo (European Union), BeiDou (China), and QZSS (Japan) constellations. The World View balloon platform was equipped with yaw control equipment to keep it from spinning during flight. After mission termination, the data was recovered and processed.

The second flight campaign was the NCL Zero Pressure Balloon Mission 1 (ZPM-1) was launched near Empire, NV on November 28, 2020 (Fig. 1d, e). The ZPM-1 balloon reached a maximum altitude of 31.7 km (104,567 ft), traveling southeast towards Utah. Overnight, ZPM-1 dropped to a lower-than-expected altitude of 17.9 km (59,000 ft) due to colder ambient temperature, which caused the balloon to drift eastwards towards the Rocky Mountains and led to termination of the mission after 12 hours. During the flight, GROOT collected balloon state data and RO data from GPS, GLONASS, Galileo, BeiDou and QZSS constellations. The payload was later recovered in southern Utah.

85 2.2 Balloon-Borne RO Measurements

Figure 2 shows the ground tracks for the two balloon flight campaigns along with the predicted occultation tangent point locations at the lowest elevation angle, labeled by their respective GNSS RO satellites. The selected occultation events extracted for analysis are highlighted for both flight campaigns. The GROOT receiver can potentially track all currently operational GNSS satellite constellations such as GPS, GLONASS, Galileo, BeiDou, and QZSS. However, due to the limited bandwidth

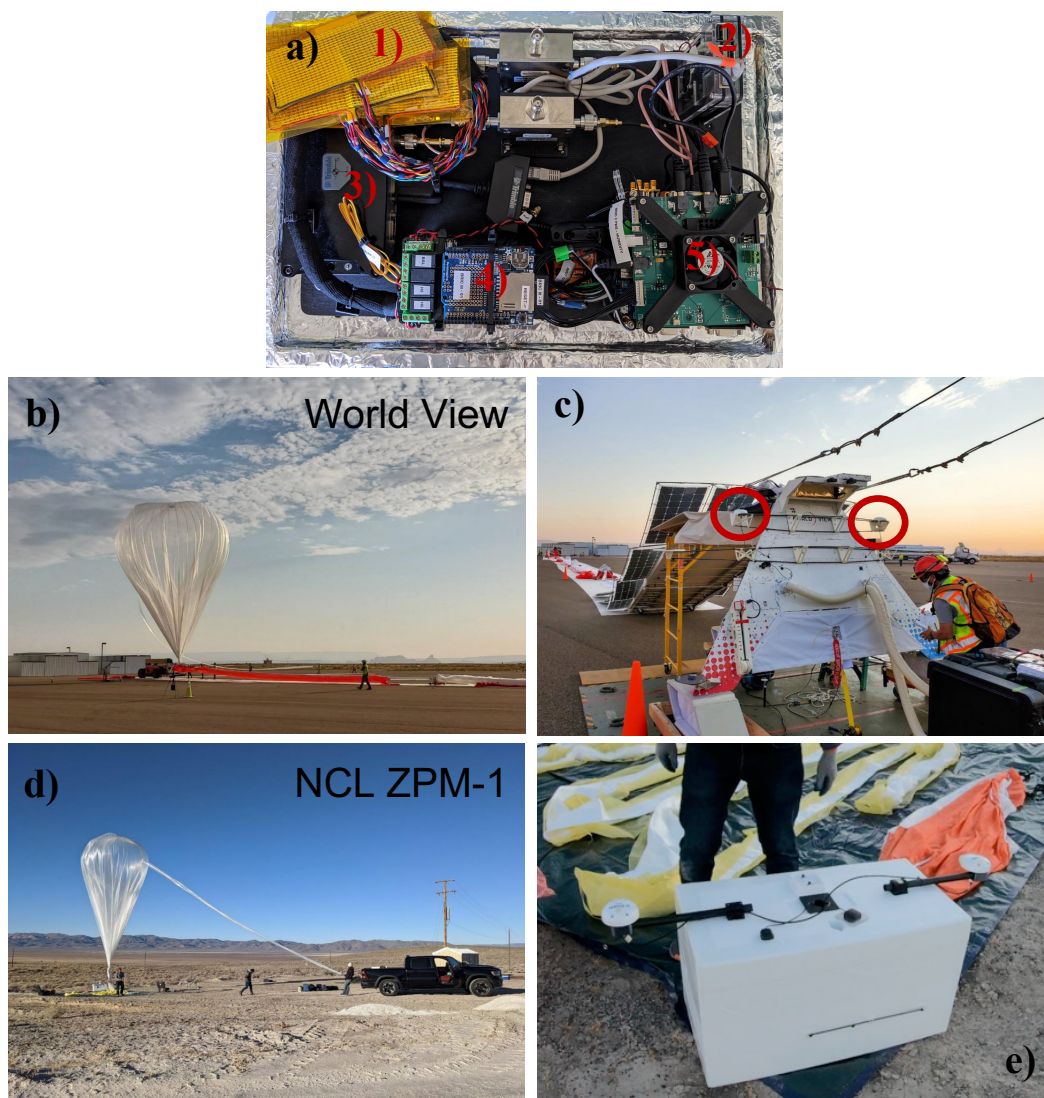


Figure 1. a) GROOT payload used in balloon RO flight missions. Numbers indicate the following components – 1) Patch heaters, 2) Raspberry Pi data logger, 3) Trimble BX992 receiver, 4) BRIC flight computer, 5) Power board/Swift Piksi Multi stack for phase and amplitude measurements (adapted from Chan et al. (2022)); b) World View Stratolite balloon being filled prior to launch. c) Balloon RO payload being prepared for launch during World View BRO flight campaigns. GNSS antennae are indicated by red circles. d) NCL ZPM balloon being filled prior to launch. e) ZPM-1 RO payload and GNSS antennae configuration.



and capability of the receiver, only the GPS signals were tracked with high enough quality. Out of a total number of 680 predicted occultation soundings for the World View flight (based on balloon and GNSS real trajectories), approximately 71% of observations came from non-GPS occultations and were not analyzed (see Fig. A1). This decision was made because GROOT processing on non-GPS satellites data from several previous flights consistently resulted in poor quality ROs. In addition, the closed-loop tracking receiver in the GROOT payload can only track setting occultations, filtering out another 50% of the available occultations. Of the remaining occultations, only the RO events having measurements with 1) minimum elevation angle less than 0° , and 2) excess phase greater than 50 meters were processed. This subset of occultations were divided into those that are good quality and those that require additional quality control such as cycle-slip corrections (Fig. A1). Of the original 680 occultations from the World View flight, only 13 good cases were extracted for analysis (see Appendix A). Similar processes were applied to ZPM-1 measurements. Unfortunately, the ZPM-1 flight encountered power failures during the segments of the flight, resulting in the loss of altitude and a much shorter flight time with fewer occultations being collected, and only 8 occultations out of 84 were selected for processing.

2.3 Balloon-Borne RO Data Processing and Retrieval Methods

After the flight data is logged, several processing steps are required to retrieve bending angle and refractivity. The full retrieval process is detailed in Chan et al. (2022), but is summarized here. The first step in the BRO retrieval is to pre-process the data for ingestion into the retrieval algorithms. Raw line-of-sight (LOS) GNSS observables, along with satellite ephemeris data, and balloon state (position/velocity) data are extracted from payload storage. Once the LOS data is parsed and aligned, the next step is to compute the excess phase by subtracting the receiver's measured phase from the LOS geometric distance between the GNSS satellite and the receiver, based on satellite ephemeris data. Step three is receiver clock calibration, where the excess phase is calibrated by differencing the excess phase of the occulting and high-elevation GNSS satellites. Step four is cycle slip correction, where an exponential curve is fitted to the data to both smooth and remove medium to large discontinuities. Step five uses a Gaussian Process Regression (GPR, Shi and Choi, 2011) to further remove smaller discontinuities. Steps three through 5 clean and smooth the excess phase data so that it can be used in the retrieval downstream in the retrieval processing. Finally, the processed result: RO excess phase, excess Doppler, SNR, and balloon state are exported as a NetCDF file, a format convenient for downstream GNSS RO retrieval processing.

To evaluate the performance of the balloon-borne GNSS-RO retrieval algorithm, an end-to-end simulation and retrieval processing system (Figure 3) originally developed for aircraft-based GNSS RO (Xie et al., 2008) was adapted for the balloon-borne RO measurements. The processing system includes four main components: (a) a geometric optics ray-tracer (i.e., Radio Occultation Simulations for Atmospheric Profiling (ROSAP, Høeg et al., 1996)), which simulates the GNSS RO signal excess phase/Doppler as it travels through a spherically symmetric atmosphere prescribed by a given atmospheric refractivity profile; (b) a module that derives the bending angle from the LOS excess phase/Doppler measurements through a modified geometric-optics (GO) retrieval (i.e., Doppler-to-alpha, (Vorob'ev and Krasil'nikova, 1994; Lesne et al., 2002; Xie et al., 2008)) and radio-holographic retrieval (i.e., full-spectrum-inversion, FSI) (Adhikari et al., 2016; Jensen et al., 2003); (c) a forward Abel integrator (FAI) that generates the bending angle profile through the forward integration of an input refractivity profile, (Fjeldbo

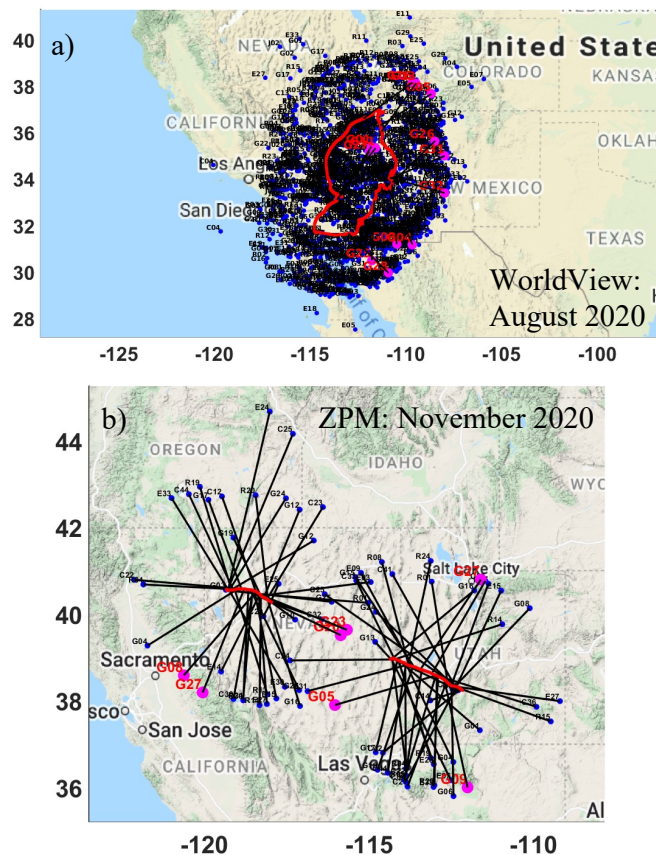


Figure 2. High-altitude balloon flight trajectory (red) and predicted occultation tangent point drifting paths and their respective GPS satellites (black) for a) World View and b) ZPM. Pink circles with red text indicate the selected RO cases and the occulting GPS satellite number presented in this study.

and Eshleman, 1969; Fjeldbo et al., 1971; Xie et al., 2008); (d) an inverse integrator that retrieves a refractivity profile via a modified Inverse Abel Transform (IAT, (Fjeldbo and Eshleman, 1969)) for airborne RO (Healy et al., 2002; Xie et al., 2008)]. Note that the GO retrieval method has limited vertical resolution and encounters multipath problems in the moist lower troposphere. Therefore, the FSI method adapted for airborne and balloon-borne RO retrieval will also be used (Adhikari et al., 2016).

After the bending angle (α) profiles are retrieved using either GO or FSI methods, the partial bending angle (α_{part}), i.e., the difference between negative and positive elevation bending angles (α_{neg} and α_{pos}) at same impact parameter, can be derived. The partial bending angle profile is then converted to the refractivity profile using the modified IAT, which requires a priori knowledge of the refractivity at the receiver during the occultation event. In addition, the local radius of curvature of the earth is also required for conversion of bending angle impact parameter to geometric height as part of the IAT. Due to the very low

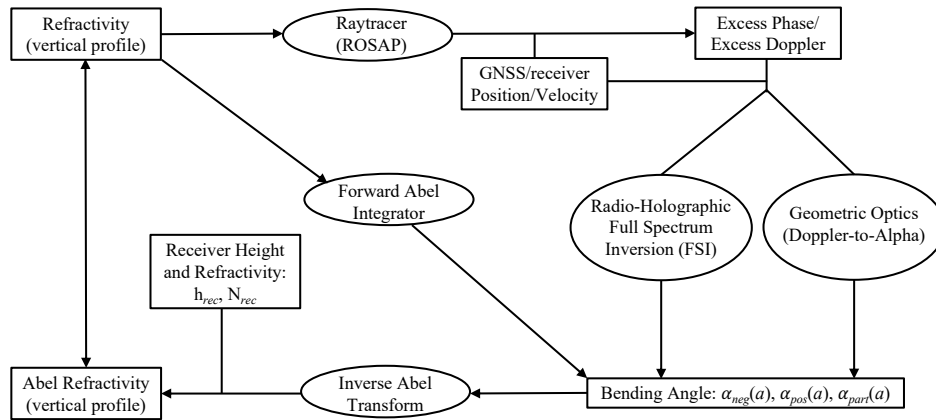


Figure 3. Flow chart of the end-to-end simulation and retrieval processing system for airborne and balloon-borne GNSS radio occultation.

excess phase delay, the raw observation of α_{pos} as well as the α_{neg} near the receiver height is generally very small and can be rather noisy, which could lead to large errors in partial bending angle and so the refractivity retrieval. Therefore, in this study, the full α_{pos} and the α_{neg} within 1.5 km below the receiver were substituted by the simulated bending angle (e.g., FAI or ROSAP bending angle simulation) based on the colocated reanalysis refractivity profile (Adhikari et al., 2016; Xie et al., 2008).

2.4 ERA5 Model Reanalysis Data

To evaluate the quality of balloon-borne RO measurements, we use 3-hourly ERA5 model reanalysis (Hersbach et al., 2020) from the European Centre for Medium-range Weather Forecasting (ECMWF) to provide estimates of atmospheric condition near the BRO sounding locations. The native ERA5 model grid has $0.25^\circ \times 0.25^\circ$ horizontal resolution and 137 vertical levels. The ERA5 profiles are referenced to geopotential heights, which are converted to geometric heights for direct comparisons to BRO profiles. The atmospheric refractivity profiles can be derived from the gridded temperature, humidity, and pressure profiles.

In addition, during an occultation event, the tangent point is located at the receiver position, when the occulting satellite is at the zero elevation. The airborne RO bending angle retrieval requires *a priori* atmospheric refractivity at the receiver, which can be provided by the colocated ERA5 profile, when high-quality in-situ measurement are not available (Xie et al., 2008). Thus, for simplicity, each occultation event uses one refractivity profile from the colocated ERA5 grid (at zero elevation tangent point location) to compute the time series of refractivity at the receiver by interpolating the refractivity profile to the receiver height at each time stamp throughout the occultation observations. Furthermore, considering the high horizontal resolution of ERA5 reanalysis and the potential fine scale variations of refractivity that are smaller than RO horizontal resolution, we use a median refractivity profile of a $1^\circ \times 1^\circ$ horizontal grid space surrounding the zero-elevation location for input into the ROSAP and FAI simulations. The tangent point locations during the occultation event can therefore be derived from ROSAP ray-tracing

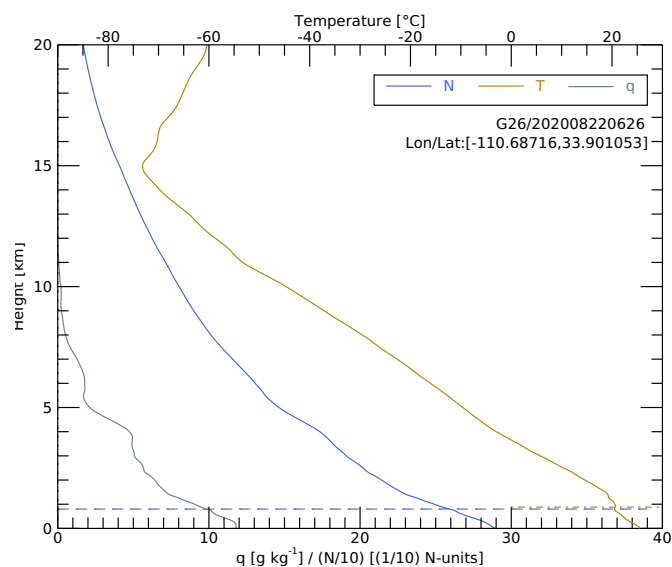


Figure 4. ERA5 vertical profiles of temperature (T , gold), specific humidity (q , grey), and refractivity (N , blue) at 0600 UTC collocated with the World View G26 BRO case on August 22, 2020. Note that for display purpose, one-tenth of the refractivity ($N/10$) was plotted. In addition, the collocation longitude and latitude of the BRO profile are indicated.

simulation with the real occultation geometry. To better evaluate the quality of BRO refractivity profile considering the large tangent point drifting distance, the ERA5 profile at the location where tangent point at a height of 5 km above mean-sea-level (MSL) will be treated as the BRO collocated profile for comparison purposes.

160 3 Case Study: BRO from the World View Campaign

Here we focus on one typical BRO sounding, an approximately 27-minute-long BRO measurement from the World View campaign (hereafter referred to as WVG26) at 06:26 UTC, August 22, 2020. The WVG26 case occurred over the Tonto National Forest, northeast of Phoenix, Arizona. The collocated ERA5 thermodynamic profiles (temperature, specific humidity, and refractivity) at the location of this BRO sounding with tangent point at 5 km above mean-sea-level are shown in Figure 4.

165 During the occultation event, the local atmosphere was hot and very dry, particularly above 5 km. Additionally, the top of the boundary layer was at approximately 0.9 km, clearly marked by a distinct temperature inversion and weak gradients in specific humidity, and refractivity (Fig. 4). The cold-point tropopause was located around 15 km altitude.

Figure 5a shows the WVG26 raw and calibrated excess phase delay observations. The calibrated excess phase delay compares favorably with the collocated ERA5-derived excess phase delay (obtained using ROSAP raytracing simulation). The high

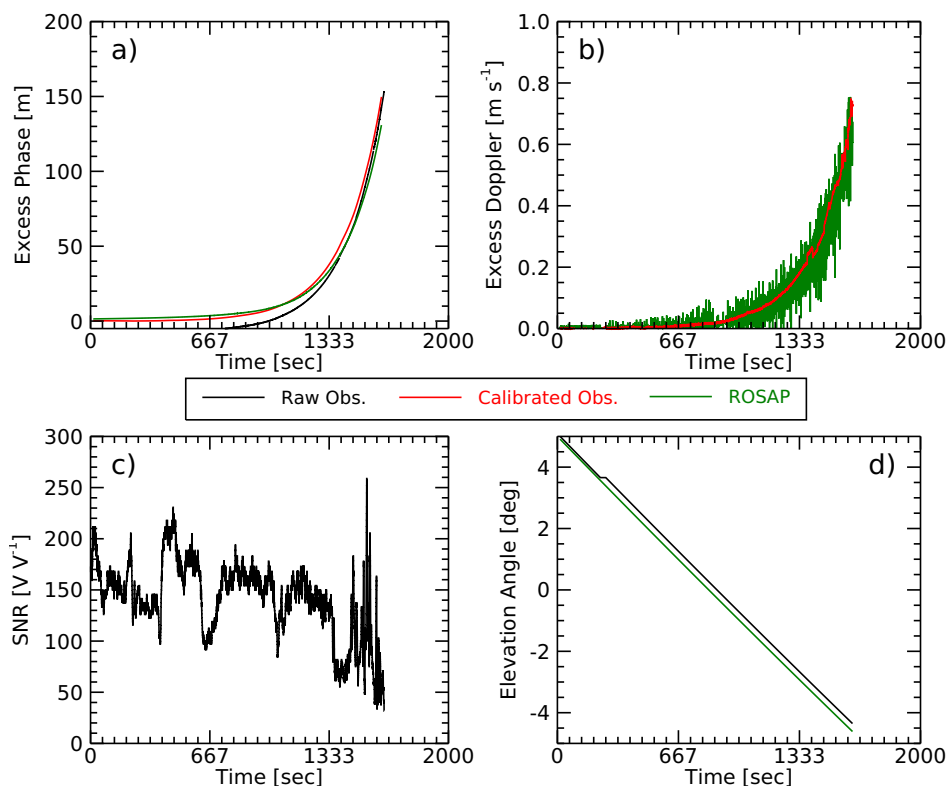


Figure 5. WVG26 time series of a) excess phase, b) excess Doppler, c) signal-to-noise ratio, and d) elevation angle from raw observations (black), calibrated observations (red), and ROSAP ray-tracing simulation (green).

170 consistency is also seen in the excess Doppler comparison (Fig. 5b) but shows larger variation in the ROSAP results, likely due
 to satellite-receiver geometry fluctuations. The observed signal-to-noise ratio (SNR) for the WVG26 case is shown in Figure
 5c. As the signal penetrates deeper into the atmosphere (i.e., the elevation angle dipping below the local horizon to approxi-
 175 mately -4.5° , Fig. 5d), the SNR typically decreases and becomes much more variable due to high signal dynamics resulting
 from the fine moisture variations in the lower troposphere. The mean SNR from the GROOT receiver (141.79 V V^{-1}) is on the
 same order of magnitude as the mean COSMIC-1 and SAC-C GNSS RO satellite missions (700 V V^{-1} , Ao et al., 2009; Ho
 et al., 2020). Considering the size of the Piksi receiver on the GROOT payload, this is quite impressive.

Given the excess phase/Doppler measurements, the accumulated bending angle from GO and FSI retrievals as a function of
 impact height (impact parameter minus the local curvature radius of the Earth) for the WVG26 case are shown in Fig. 6a. Note
 that the noisy α_{pos} and α_{neg} within 1.5 km below the receiver height were replaced by the simulated FAI bending angle based
 180 on the colocated ERA5 refractivity profile (Fig. 4). Fig. 6a also shows a conceptual calculation of the partial bending angle as
 discussed in Section 2b. At each impact height, α_{pos} is subtracted from α_{neg} to calculate α_{part} , which is later used to retrieve

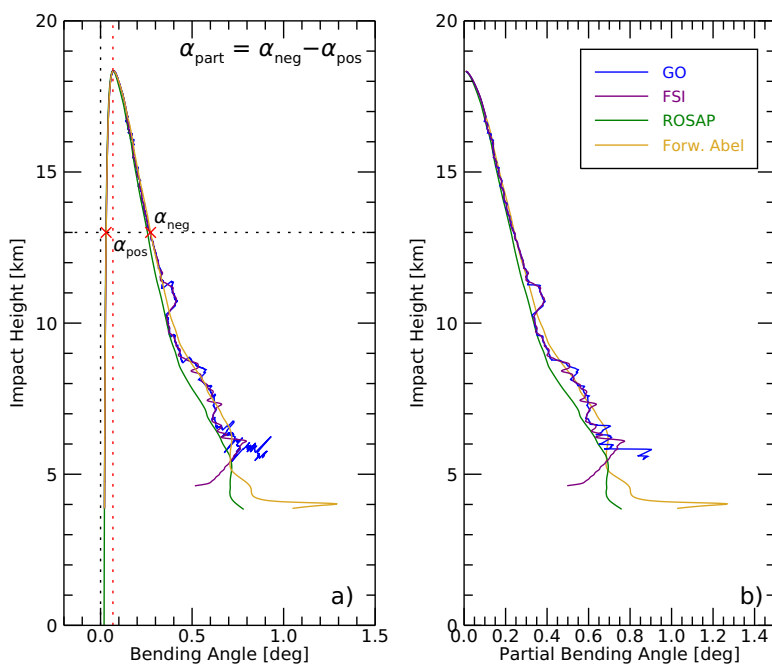


Figure 6. a) Bending angle for WVG26 case from the GO retrieval (blue) and FSI retrieval (purple), in comparison with the colocated ERA5 bending angle from ROSAP ray-tracing simulation (green), and forward-Abel-integrator (gold). Conceptual calculation of partial bending angle at 13 km impact height is also shown. b) Final partial bending angle for WVG26 case from the GO retrieval (blue), FSI retrieval (purple), ROSAP ray-tracing simulation (green), and Forward Abel transform (gold).

the final refractivity profile. Figure 6b shows the partial bending angle calculated using the method shown in Fig. 6a with 100 m log-linear vertical smoothing applied. It is worth noting that BRO bending angle observations from both the GO and FSI retrievals match the colocated ERA5 FAI and ROSAP simulations quite well from the balloon altitude (just over 18 km) all the way down to impact heights of around 6 km (corresponding to approximately 4 km above MSL, Fig. 6).

Figure 7a shows the refractivity retrieval for the WVG26 BRO case. The 5 km tangent height ERA5 refractivity profiles colocated with the WVG26 case is approximately 425 km from the receiver location, and the terrain changes significantly compared to the origin point in the Tonto National Forest. From the top of the refractivity profiles, both the GO and FSI retrievals match the ERA5 refractivity profile from the location of the 5 km tangent height very well. Similar to the α_{part} results, the refractivity retrieval from FSI bending angle reaches about 1 km deeper into the atmosphere than the GO retrieval, highlighting the usefulness of the FSI over GO methods. This is primarily due to the improvement from FSI on resolving the multipath problem over the GO method in the moist lower troposphere.

In order to quantify the differences between the retrievals and the colocated ERA5 profile, the fractional refractivity difference profile is calculated. Figure 7b shows the fractional refractivity difference between the GO/FSI retrievals and the colocated

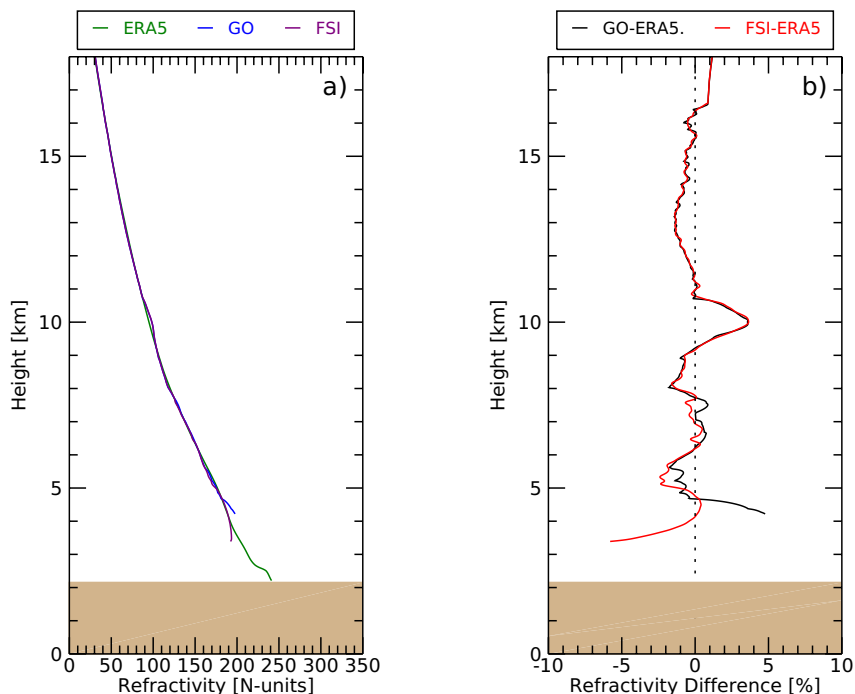


Figure 7. a) BRO refractivity retrieval for WVG26 case from GO (blue) and FSI (purple) compared to the colocated refractivity profile from ERA5. b) Fractional refractivity difference between BRO retrieval and ERA5 (GO, black; FSI, red). Local terrain at the location of BRO tangent point at 5 km above MSL is marked by tan polygons.

195 ERA5 profiles, respectively. The GO retrieval is highly consistent with FSI retrieval above ~ 7.5 km and start showing small differences below. Above 10 km, the median differences between the retrievals and the colocated 5 km tangent height ERA5 profile are both -0.27% to -0.26% with a median-absolute-deviation (MAD) of approximately 0.62% . Both retrievals continue to perform very well in the middle troposphere, between 5 km and 10 km with median/MAD refractivity differences of $-0.21 \pm 0.74\%$ for the GO retrieval and $-0.38 \pm 0.59\%$ for the FSI retrieval. Once more water vapor is encountered below 5 km
 200 altitude, the magnitude of the difference for the GO retrieval increases to $1.67 \pm 2.12\%$. The refractivity difference for the FSI retrieval remains comparable to the higher altitude overall refractivity difference estimates at $-0.24 \pm 0.57\%$.

4 Evaluation of Balloon-Borne RO Refractivity Retrievals

Figure 8 shows the fractional refractivity difference between GO/FSI retrievals and the colocated ERA5 profile for each BRO sounding from the World View flight campaign. Summary statistics for the World View flight campaign are shown in Table
 205 1. The median refractivity difference between the GO retrieval and the colocated ERA5 oscillates within 0.25% with MAD

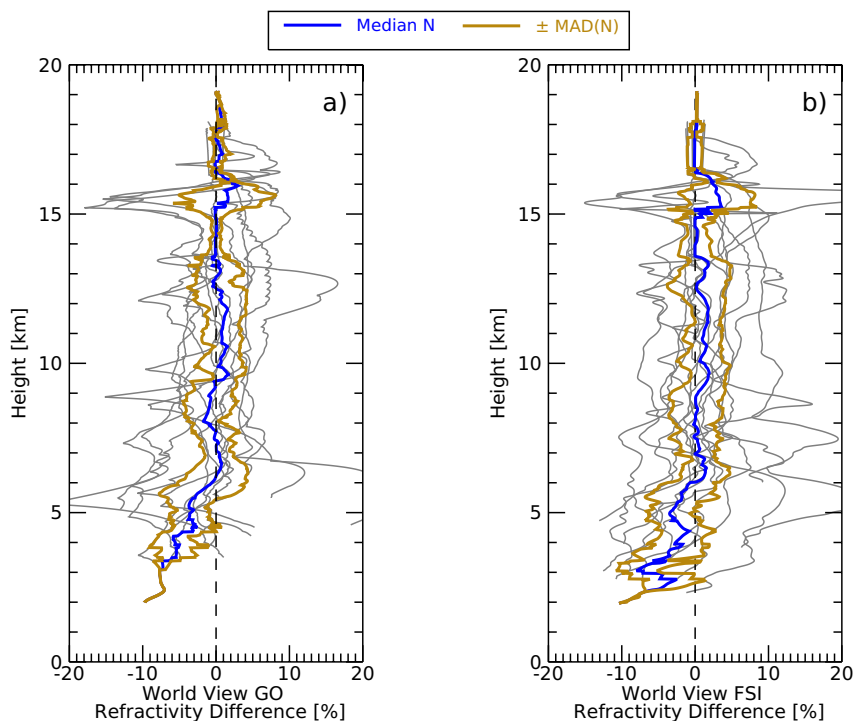


Figure 8. Fractional refractivity difference between BRO retrievals and the colocated ERA5 for: a) GO retrievals and b) FSI retrievals of all World View cases (grey). The median fractional refractivity difference profiles are shown in blue and the median \pm the median absolute deviation (MAD) is shown in gold

Table 1. Summary statistics for the World View flight campaign over varying height ranges. Median refractivity differences are shown with the corresponding median absolute deviation over the same height range.

Height Range [km]	GO Median N Difference [%]	FSI Median N Difference [%]
0-5	-5.86 ± 1.99	-3.60 ± 3.26
5-10	-0.25 ± 2.97	0.32 ± 3.06
10-15	0.57 ± 2.44	1.06 ± 2.29
15-20	0.53 ± 0.71	0.23 ± 0.94
Overall	0.03 ± 2.28	0.24 ± 2.61

between 0.71% above 15 km and approximately 2.28% across all levels (see Table 1). The GO refractivity retrieval starts showing negative N -bias below approximately 6 km, with the minimum bias with a median difference of -5.86% (MAD: 1.99%) over the 0-5 km height range. The FSI retrieval also starts showing negative N -bias below approximately 6 km, but with a smaller median difference of -3.60% (MAD: 3.26%).

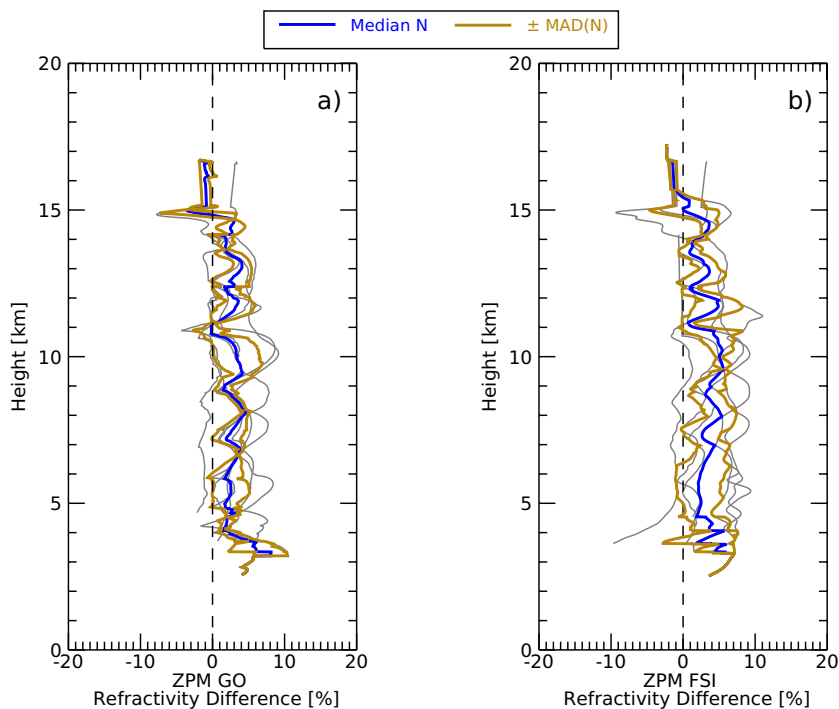


Figure 9. Same as Figure 8, but for the ZPM-1 flight campaign.

210 The lowest level negative N -bias is likely caused by the tracking errors (e.g., cycle slips) introduced by the closed-loop tracking receiver, which could degrade the BRO observation quality. Furthermore, high spatial variations in moisture content can also cause low SNR or high signal dynamics ultimately resulting in a negative bending angle bias (Wang et al., 2016).

Figure 9 shows the fractional refractivity difference profiles for the ZPM-1 flight campaign from the GO and FSI retrievals. The ZPM-1 refractivity difference shows much more variability and is slightly positively biased compared to the World View
215 campaign data. The GO retrieval has an overall median refractivity difference of 2.57% (MAD: 1.38%). The maximum N -bias from the GO retrieval is 4.05% in the lower troposphere. The FSI retrieval has an overall median refractivity difference of 3.13% (MAD: 2.03%). The World View platform had rotational yaw control capability, whereas the ZPM-1 platform did not – as such, the platform and GNSS antennae were free to spin during high-altitude wind gusts. During RO events, rotational movement induced position errors in the dual-antenna navigation system, which could result in higher noise and larger N -bias
220 and warrants future investigation.

The limitations of closed-loop tracking receivers may also affect the BRO refractivity retrieval quality. Wang et al. (2016) found that the low SNR in the airborne GNSS RO observations could result in approximately $\pm 5\%$ refractivity error. This is consistent with the overall results showed here, meaning that an improvement to SNR in the lower atmosphere would be extremely beneficial. However, it is important to note that despite the overall positive bias in the ZPM-1 cases, the median



Table 2. Same as Table 1, but for the ZPM-1 flight campaign.

Height Range [km]	GO Median <i>N</i> Difference [%]	FSI Median <i>N</i> Difference [%]
0-5	4.05 ± 0.99	4.01 ± 2.15
5-10	2.94 ± 1.56	3.59 ± 2.29
10-15	2.57 ± 1.78	3.03 ± 1.73
15-20	-0.94 ± 0.64	-1.33 ± 0.47
Overall	2.57 ± 1.38	3.13 ± 2.03

225 absolute deviation of the cases minimizes in the upper and middle troposphere, much like the World View campaign data. One
important caveat for the ZPM-1 campaign data is the small number of available occultations. Power loss issues on the platform
during the flights caused a decrease in the number of occultations. The low sampling numbers could also lead to larger median
refractivity differences.

5 Conclusions

230 In this study, the GNSS RO atmospheric profiling technique has been adapted for use on high-altitude balloon platforms.
Most of the past airborne and balloon-borne RO payloads require custom made parts and costly operational expenses that
require significant investments. We show the successful implementation of the Night Crew Labs GROOT payload developed
from commercial off-the-shelf components on high-altitude balloon platforms. This approach is simpler and significantly more
affordable than their current airborne and space-based methods. The results from the low-cost, highly compact GROOT payload
235 are promising.

Utilizing a balloon platform for GNSS RO observations has been done only once in the past. Haase et al. (2012) showed
the proof-of-concept for balloon-borne GNSS RO using a custom-built receiver and found excess Doppler agreement that
would correspond to approximately 1% refractivity difference. The BRO retrievals from the GROOT payload have refractivity
differences in the middle and upper troposphere comparable to previous airborne and balloon-borne RO studies (Adhikari et al.,
240 2016; Haase et al., 2012; Healy et al., 2002; Xie et al., 2008). The added benefit of using BRO platforms is the dense spatial
sampling available due to the low platform velocities relative to the LEO-based RO satellites. Additionally, BRO platforms are
scalable and can potentially be launched in advance of significant weather events and remain aloft for long periods of time to
collect abundant RO observations.

Currently, the major limitation of BRO platforms with COTS payloads is the use of closed-loop tracking GNSS receiver,
245 which is commercially available. For GNSS RO purposes, closed-loop tracking can limit penetration of retrieved refractivity
profiles into the lower troposphere due to the large variations in moisture content. Additionally, closed-loop tracking also
prohibits the tracking of rising occultations, cutting the potential number of RO soundings in half. For these reasons, design
and implementation of COTS payloads capable of open-loop tracking is the next natural step to improving balloon-borne RO.
Furthermore, BRO platform orientation can be uncontrolled, so a sudden change in winds aloft can alter the antenna position



250 and cause signal loss. Additionally, the comparatively slow-moving receivers result in longer occultations (approximately 20-30 minutes for one balloon-borne RO event, in comparison to ~1 minute for one spaceborne RO event), which can result in larger unwrapping error (Wang et al., 2016) and lead to further underestimates of bending angle in the moist lower troposphere.

An analysis of the quality of the retrieved refractivity profiles reveals that the median refractivity difference for the World View campaign is generally less than 1%. The same analysis of the ZPM-1 campaign data shows that the median is slightly
255 positively biased overall (approximately 3%), but with similar median absolute deviation values. While both GO and FSI retrieval methods offer promising results, it appears that the FSI retrievals tend to outperform the GO retrievals in terms of atmospheric penetration. The limitation of the close-loop tracking could be the primary cause of the negative N-bias below 6 km as seen in World View BRO soundings. In addition, the relatively low SNR in the lower troposphere could also lead to negative bending angle bias, which could also be another likely cause of the negative refractivity bias in the lower troposphere.

260 Overall, we show that high-altitude balloons with RO payloads can be launched in all weather conditions, over areas of complex terrain, and can potentially remain aloft for far longer than airborne RO platforms. Therefore, the balloon-borne RO platform can offer unprecedented high spatial and temporal BRO sampling over targeted regions far higher than traditional spaceborne RO (see Fig. 2). Additionally, balloon-borne RO data could be much more cost effective to retrieve due to the low-cost COTS GNSS receiver and overall affordability of the high-altitude balloon flight platform, as the instrument
265 can be retrieved and reused after each deployment. We believe the advances on the COTS GNSS receiver development and high-altitude balloon platform control in the future will lead to large increases in high-quality localized BRO soundings over targeting weather events (e.g., severe thunderstorms etc.) and improve regional weather forecasts through data assimilation.

Data availability. TAMUCC-derived balloon-borne RO data and retrievals used in this study are publicly available from the NOAA National Center for Environmental Information under CC-BY-NC-SA 4.0 licensing (Nelson et al., 2022). TAMUCC-derived balloon-borne RO data
270 and retrievals are also available upon request by contacting Kevin Nelson at knelson12@islander.tamucc.edu. NCL derived balloon-borne RO data and retrievals used in this study are available upon request by contacting Bryan Chan at bryan@nightcrewlabs.com.

All ERA5 data (Hersbach et al., 2020) are available to download from ECMWF and CDS with proper registration and credentials. Instructions for download can be found in: <https://confluence.ecmwf.int/display/CKB/How+to+download+ERA5>.

Appendix A: Balloon-Borne RO Cases and Sampling

275 Balloon-borne RO can collect high density observations around the platform, particularly compared to spaceborne RO. As was discussed in Section 2.1, the Piksi GNSS receiver onboard World View balloon could observe a predicted total of 680 potential occultations. Because of frequency restrictions built into the Piksi receiver, signals from GLONASS, BeiDou, QZSS, and Galileo are less reliable due to slight frequency differences compared to the GPS system.

Figure A1 shows a Sankey plot filtering visualization of the World View predicted occultations. Of the original 680 predicted
280 ROs, a total of 485 were incomplete from all available GNSS satellite constellations. The remaining 195 occultations then filter further by removing those from QZSS, Galileo, BeiDou, and GLONASS with low quality due to the frequency tuning inherent

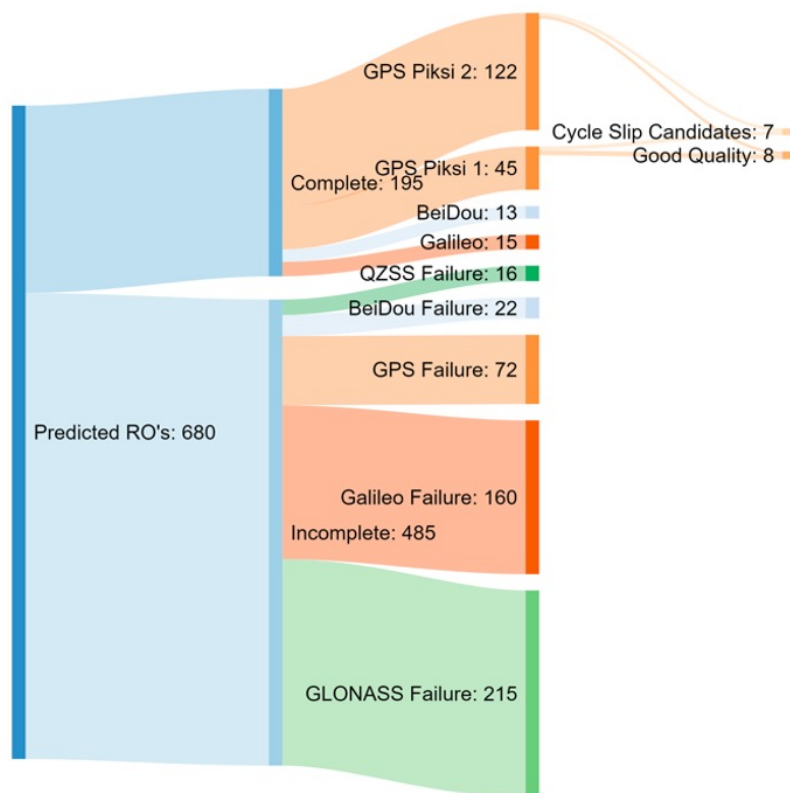


Figure A1. Sankey filtering plot visualizing the balloon-borne RO case filtering.

to the Piksi receiver. Of the 167 from the GPS system, only 8 good quality cases were ready to use immediately. Another 7 cases required some pre-processing in the form of cycle-slip corrections. During post-processing, 4 cases were removed for various quality control reasons, leaving the final 11 cases presented in Section 4. The same process was also applied for cases
285 observed during the ZPM-1 flight campaign.

Author contributions. Authors BC and FX developed the concept for the study. Authors BC, AG, TR, PT, JK, and CS completed payload engineering. BC, FX, and AG developed the methodology for the study. KN, FX, JK, and AG developed software used for this study. KN, BC, JK, and AG completed data validation at different steps. Formal analysis was completed by KN, JK, AG, and FX. Data curation was done by KN. Data visualization was done by KN, JK, and AG. Initial drafts of this manuscript were written by KN. Editing and review of the
290 manuscript was completed by KN, FX, BC, and TR. Project administration, funding acquisition, and supervision were done by BC and FX.

Competing interests. The authors declare no conflicts of interest or competing interests.



Acknowledgements. This paper is supported by NOAA grant (1305M2-19-C-NRMW-0015). Author K. Nelson acknowledges the research assistantship support from Coastal Marine System Science Program at Texas A&M University – Corpus Christi. Authors from Night Crew Labs acknowledge additional support from NASA grant 80NSSC20K0106. The authors would also like to thank Dr. Loknath Adhikari from the University of Maryland for productive discussion. The anonymous reviewers are also acknowledged for their insight and comments to improve this paper.



References

- Adhikari, L., Xie, F., and Haase, J. S.: Application of the full spectrum inversion algorithm to simulated airborne GPS radio occultation signals, *Atmospheric Measurement Techniques*, 9, 5077–5087, <https://doi.org/10.5194/amt-9-5077-2016>, 2016.
- 300 Anthes, R. A., Bernhardt, P. A., Chen, Y., Cucurull, L., Dymond, K. F., Ector, D., Healy, S. B., Ho, S. P., Hunt, D. C., Kuo, Y. H., Liu, H., Manning, K., McCormick, C., Meehan, T. K., Randel, W. J., Rocken, C., Schreiner, W. S., Sokolovskiy, S. V., Syndergaard, S., Thompson, D. C., Trenberth, K. E., Wee, T. K., Yen, N. L., and Zeng, Z.: The COSMIC/FORMOSAT-3 Mission: Early Results, *Bulletin of the American Meteorological Society*, 89, 313–334, <https://doi.org/10.1175/bams-89-3-313>, 2008.
- Ao, C. O., Hajj, G. A., Meehan, T. K., Dong, D., Iijima, B. A., Mannucci, A. J., and Kursinski, E. R.: Rising and setting GPS occultations by use of open-loop tracking, *Journal of Geophysical Research*, 114, <https://doi.org/10.1029/2008jd010483>, 2009.
- 305 Boullot, N., Rabier, F., Langland, R., Gelaro, R., Cardinali, C., Guidard, V., Bauer, P., and Doerenbecher, A.: Observation impact over the southern polar area during the Concordiasi field campaign, *Quarterly Journal of the Royal Meteorological Society*, 142, 597–610, <https://doi.org/10.1002/qj.2470>, 2014.
- Bowler, N. E.: An assessment of GNSS radio occultation data produced by Spire, *Quarterly Journal of the Royal Meteorological Society*, 310 146, 3772–3788, <https://doi.org/10.1002/qj.3872>, 2020.
- Carreno-Luengo, H., Camps, A., Querol, J., and Forte, G.: First Results of a GNSS-R Experiment From a Stratospheric Balloon Over Boreal Forests, *IEEE Transactions on Geoscience and Remote Sensing*, 54, 2652–2663, <https://doi.org/10.1109/tgrs.2015.2504242>, 2016.
- Chan, B. C., Goel, A., Kosh, J., Reid, T. G. R., Snyder, C. R., Tarantino, P. M., Soedarmadji, S., Soedarmadji, W., Nelson, K. J., Xie, F., and Vergalla, M.: GNSS Radio Occultation on Aerial Platforms with Commercial Off-the-Shelf Receivers, *ION GNSS Proceedings*, 315 <https://arxiv.org/abs/2109.13328>, 2021.
- Chan, B. C., Goel, A., Kosh, J., Reid, T. G. R., Snyder, C. R., Tarantino, P. M., Soedarmadji, S., Soedarmadji, W., Nelson, K. J., Xie, F., and Vergalla, M.: Commercial GNSS Radio Occultation on Aerial Platforms with Off-The-Shelf Receivers, *Navigation*, 2022.
- Fjeldbo, G. and Eshleman, V. R.: Atmosphere of Venus as Studied with the Mariner 5 Dual Radio-Frequency Occultation Experiment, *Radio Science*, 4, 879–897, <https://doi.org/10.1029/RS004i010p00879>, 1969.
- 320 Fjeldbo, G., Kliore, A. J., and Eshleman, V. R.: The neutral atmosphere of Venus as studied with the Mariner V radio occultation experiments, *The Astronomical Journal*, 76, 123, 1971.
- Garrison, J. L., Walker, M., Haase, J. S., Lulich, T., Xie, F., Ventre, B., Boehme, M. H., Wilmhoff, B., and Katzberg, S. J.: Development and Testing of the GISMOS Instrument, *IEEE International*, 2007.
- Gelaro, R.: GEOS-5 Data Assimilation and Forecast Impacts for Concordiasi, in: THORPEX DAOS Working Group, 2011.
- 325 Haase, J. S., Maldonado-Vargas, J., Rabier, F., Cocquerez, P., Minois, M., Guidard, V., Wyss, P., and Johnson, A. V.: A proof-of-concept balloon-borne Global Positioning System radio occultation profiling instrument for polar studies, *Geophysical Research Letters*, 39, n/a–n/a, <https://doi.org/10.1029/2011gl049982>, 2012.
- Harnisch, F., Healy, S. B., Bauer, P., and English, S. J.: Scaling of GNSS Radio Occultation Impact with Observation Number Using an Ensemble of Data Assimilations, *Monthly Weather Review*, 141, 4395–4413, <https://doi.org/10.1175/mwr-d-13-00098.1>, 2013.
- 330 Healy, S. B., Haase, J. S., and Lesne, O.: Abel transform inversion of radio occultation measurements made with a receiver inside the Earth’s atmosphere, *Annales Geophysicae*, 20, 2002.
- Hersbach, H., Bell, B., Berrisford, P., Hirahara, S., Horányi, A., Muñoz-Sabater, J., Nicolas, J., Peubey, C., Radu, R., Schepers, D., Simmons, A., Soci, C., Abdalla, S., Abellan, X., Balsamo, G., Bechtold, P., Biavati, G., Bidlot, J., Bonavita, M., De Chiara, G., Dahlgren, P., Dee,



- D., Diamantakis, M., Dragani, R., Flemming, J., Forbes, R., Fuentes, M., Geer, A., Haimberger, L., Healy, S., Hogan, R. J., Hólm, E.,
335 Janisková, M., Keeley, S., Laloyaux, P., Lopez, P., Lupu, C., Radnoti, G., de Rosnay, P., Rozum, I., Vamborg, F., Villaume, S., and Thépaut,
J.-N.: The ERA5 Global Reanalysis, *Quarterly Journal of the Royal Meteorological Society*, n/a, <https://doi.org/10.1002/qj.3803>, 2020.
- Ho, S.-P., Zhou, X., Shao, X., Zhang, B., Adhikari, L., Kireev, S., He, Y., Yoe, J. G., Xia-Serafino, W., and Lynch, E.: Initial Assessment of
the COSMIC-2/FORMOSAT-7 Neutral Atmosphere Data Quality in NESDIS/STAR Using In Situ and Satellite Data, *Remote Sensing*,
12, <https://doi.org/10.3390/rs12244099>, 2020.
- 340 Høeg, P., Hauchecorne, A., Kirchengast, G., Syndergaard, S., Belloul, B., Leitinger, R., and Rothleitner, W.: Derivation of Atmospheric
Properties using a Radio Occultation Technique, Report 95-4, Danish Meteorological Institute, 1996.
- Imamura, T., Ando, H., Tellmann, S., Pätzold, M., Häusler, B., Yamazaki, A., Sato, T. M., Noguchi, K., Futaana, Y., Oshlisniok, J., Limaye,
S., Choudhary, R. K., Murata, Y., Takeuchi, H., Hirose, C., Ichikawa, T., Toda, T., Tomiki, A., Abe, T., Yamamoto, Z.-i., Noda, H., Iwata,
T., Murakami, S.-y., Satoh, T., Fukuhara, T., Ogohara, K., Sugiyama, K.-i., Kashimura, H., Ohtsuki, S., Takagi, S., Yamamoto, Y., Hirata,
345 N., Hashimoto, G. L., Yamada, M., Suzuki, M., Ishii, N., Hayashiyama, T., Lee, Y. J., and Nakamura, M.: Initial performance of the radio
occultation experiment in the Venus orbiter mission Akatsuki, *Earth, Planets and Space*, 69, <https://doi.org/10.1186/s40623-017-0722-3>,
2017.
- Jensen, A. S., Lohmann, M. S., Benzon, H.-H., and Nielsen, A. S.: Full Spectrum Inversion of radio occultation signals, *Radio Science*, 38,
n/a–n/a, <https://doi.org/10.1029/2002rs002763>, 2003.
- 350 Kliore, A. J., Cain, D. L., Fjeldbo, G., Seidel, B. L., Sykes, M. J., and Rasool, S. I.: The Atmosphere of Mars from Mariner 9 Radio
Occultation Measurements, *Icarus*, 17, 484–516, 1972.
- Kursinski, E. R., Hajj, G. A., Bertiger, W. I., Leroy, S. S., Meehan, T. K., Romans, L. J., Schofield, J. T., McCleese, D. J., Melbourne, W. G.,
Thornton, C. L., Yunck, T. P., Eyre, J. R., and Nagafini, R. N.: Initial Results of Radio Occultation Observations of Earth's Atmosphere
Using the Global Positioning System, *Science*, 271, 1107–1110, 1996.
- 355 Kursinski, E. R., Hajj, G. A., Schofield, J. T., Linfield, R. P., and Hardy, K. R.: Observing Earth's atmosphere with radio occul-
tation measurements using the Global Positioning System, *Journal of Geophysical Research: Atmospheres*, 102, 23 429–23 465,
<https://doi.org/10.1029/97jd01569>, 1997.
- Lesne, O., Haase, J. S., Kirchengast, G., Ramsauer, J., and Poetzi, W.: Sensitivity analysis for airborne sounding of the troposphere by GNSS
radio occultation, *Physics and Chemistry of the Earth*, 27, 2002.
- 360 Lindal, G. F.: The atmosphere of Neptune-an analysis of radio occultation data acquired with Voyager 2, *The Astronomical Journal*, 103,
967–982, 1992.
- Lindal, G. F., Hotz, H. B., Sweetnam, D. N., Shippony, Z., Brenkle, J. P., Hartsell, G. V., Spear, R. T., and Michael, W. H.: Viking radio occul-
tation measurements of the atmosphere and topography of Mars: Data acquired during 1 Martian year of tracking, *Journal of Geophysical
Research*, 84, <https://doi.org/10.1029/JB084iB14p08443>, 1979.
- 365 Luntama, J.-P., Kirchengast, G., Borsche, M., Foelsche, U., Steiner, A., Healy, S., von Engel, A., O'Clérigh, E., and Marquardt, C.: Prospects
of the EPS GRAS Mission for Operational Atmospheric Applications, *Bulletin of the American Meteorological Society*, 89, 1863–1875,
<https://doi.org/10.1175/2008BAMS2399.I>, 2008.
- Murphy, B. J., Haase, J. S., Muradyan, P., Garrison, J. L., and Wang, K. N.: Airborne GPS radio occultation refractivity profiles observed
in tropical storm environments, *Journal of Geophysical Research: Atmospheres*, 120, 1690–1709, <https://doi.org/10.1002/2014jd022931>,
370 2015.



- Nelson, K. J., Xie, F., Chan, B. C., Goel, A., Kosh, J., Reid, T. G. R., Snyder, C. R., and Tarantino, P. M.: GNSS Radio Occultation Sounding from Commercial Off-the-Shelf Receivers onboard Balloon Platforms, 2022.
- Rabier, F., Bouchard, A., Brun, E., Doerenbecher, A., Guedj, S., Guidard, V., Karbou, F., Peuch, V.-H., El Amraoui, L., Puech, D., Genthon, C., Picard, G., Town, M., Hertzog, A., Vial, F., Cocquerez, P., Cohn, S. A., Hock, T., Fox, J., Cole, H., Parsons, D., Powers, J., Romberg, K., VanAndel, J., Deshler, T., Mercer, J., Haase, J. S., Avallone, L., Kalnajs, L., Mechoso, C. R., Tangborn, A., Pellegrini, A., Frenot, Y., Thépaut, J.-N., McNally, A., Balsamo, G., and Steinle, P.: The Concordiasi Project in Antarctica, *Bulletin of the American Meteorological Society*, 91, 69–86, <https://doi.org/10.1175/2009bams2764.1>, 2010.
- Rabier, F., Cohn, S., Cocquerez, P., Hertzog, A., Avallone, L., Deshler, T., Haase, J., Hock, T., Doerenbecher, A., Wang, J., Guidard, V., Thépaut, J.-N., Langland, R., Tangborn, A., Balsamo, G., Brun, E., Parsons, D., Bordereau, J., Cardinali, C., Danis, F., Escarnot, J.-P., Fourrié, N., Gelaro, R., Genthon, C., Ide, K., Kalnajs, L., Martin, C., Meunier, L.-F., Nicot, J.-M., Perttula, T., Potts, N., Ragazzo, P., Richardson, D., Sosa-Sesma, S., and Vargas, A.: The Concordiasi Field Experiment over Antarctica: First Results from Innovative Atmospheric Measurements, *Bulletin of the American Meteorological Society*, 94, ES17–ES20, <https://doi.org/10.1175/bams-d-12-00005.1>, 2013.
- Ruston, B. and Healy, S.: Forecast Impact of FORMOSAT-7/COSMIC-2 GNSS Radio Occultation Measurements, *Atmospheric Science Letters*, 22, <https://doi.org/10.1002/asl.1019>, 2020.
- Schreiner, W. S., Weiss, J. P., Anthes, R. A., Braun, J., Chu, V., Fong, J., Hunt, D., Kuo, Y. H., Meehan, T., Serafino, W., Sjoberg, J., Sokolovskiy, S., Talaat, E., Wee, T. K., and Zeng, Z.: COSMIC-2 Radio Occultation Constellation: First Results, *Geophysical Research Letters*, 47, <https://doi.org/10.1029/2019gl086841>, 2020.
- Shi, J. Q. and Choi, T.: *Gaussian Process Regression Analysis for Functional Data*, CRC Press, Boca Raton, FL, USA, 2011.
- Vorob'ev, V. V. and Krasil'nikova, T. G.: Estimation of the Accuracy of the Atmospheric Refractive Index Recovery from Doppler Shift Measurements at Frequencies Used in the NAVSTAR System, *Physics of the Atmosphere and Ocean*, 29, 1994.
- Wang, K.-N., Garrison, J. L., Acikoz, U., Haase, J. S., Murphy, B. J., Muradyan, P., and Lulich, T.: Open-Loop Tracking of Rising and Setting GPS Radio-Occultation Signals From an Airborne Platform: Signal Model and Error Analysis, *IEEE Transactions on Geoscience and Remote Sensing*, 54, 3967–3984, <https://doi.org/10.1109/tgrs.2016.2532346>, 2016.
- Wang, K.-N., Garrison, J. L., Haase, J. S., and Murphy, B. J.: Improvements to GPS Airborne Radio Occultation in the Lower Troposphere Through Implementation of the Phase Matching Method, *Journal of Geophysical Research: Atmospheres*, 122, <https://doi.org/10.1002/2017jd026568>, 2017.
- Ware, R. H., Exner, M., Feng, D., Gorbunov, M., Hardy, K. R., Herman, B., Kuo, Y. H., Meehan, T. K., Melbourne, W., Rocken, C., Schreiner, W. S., Sokolovskiy, S., Solheim, F., Zou, X., Anthes, R., Businger, S., and Trenberth, K. E.: GPS Sounding of the Atmosphere from Low Earth Orbit: Preliminary Results, *Bulletin of the American Meteorological Society*, 77, 19–40, 1996.
- Xie, F., Haase, J. S., and Syndergaard, S.: Profiling the Atmosphere Using the Airborne GPS Radio Occultation Technique: A Sensitivity Study, *IEEE Transactions on Geoscience and Remote Sensing*, 46, 3424–3435, <https://doi.org/10.1109/tgrs.2008.2004713>, 2008.
- Zuffada, C., Hajj, G. A., and Kursinski, E. R.: A novel approach to atmospheric profiling with a mountain-based or airborne GPS receiver, *Journal of Geophysical Research: Atmospheres*, 104, 24 435–24 447, <https://doi.org/10.1029/1999jd900766>, 1999.